Article:
Lyons, T.P., Gillard, D.J. orcid.org/0000-0002-0001-4918, Leblanc, C. et al. (11 more authors) (2022) Giant effective Zeeman splitting in a monolayer semiconductor realized by spin-selective strong light–matter coupling. Nature Photonics, 16 (9). pp. 632-636. ISSN 1749-4885

https://doi.org/10.1038/s41566-022-01025-8

---

nature portfolio

https://doi.org/10.1038/s41566-022-01025-8

Supplementary information

Giant effective Zeeman splitting in a monolayer semiconductor realized by spin-selective strong light–matter coupling

In the format provided by the authors and unedited

Supplementary Information for: Giant effective Zeeman splitting in a monolayer semiconductor realized by spin-selective strong light-matter coupling

Supplementary Note 1: Electron density calculations

We estimate the free electron density in our $MoSe_2$ monolayer by following the treatment described by Roch, *et al.* for MoS_2 [1], itself motivated by earlier works by Suris, *et al.* [2], in which exciton absorption in the presence of a 2DEG was considered. In this treatment, the absorption of the system may be described by two exciton-electron scattering mechanisms, that of a singlet or triplet interaction between the 2DEG and the photogenerated exciton. Two scattering matrix elements, T_s and T_t respectively, can therefore be written as [1, 2]:

$$T_s(\hbar\omega + E) = \frac{2\pi\hbar^2}{\mu_T} \frac{1}{\ln\left(\frac{-E_b(X^-)}{(\hbar\omega+E)-E(X^0)+i\gamma}\right)} \tag{S1}$$

$$T_t(\hbar\omega + E) = \frac{2\pi\hbar^2}{\mu_T} \frac{1}{\ln\left(\frac{-E_b(X^0)}{(\hbar\omega+E)-E(X^0)+i\gamma}\frac{E_b(X^0)}{E_b(X^-)}\right)} \tag{S2}$$

where $E_b(X^0)$ and $E_b(X^-)$ are the exciton and trion binding energies, $E(X^0)$ is the exciton energy, γ is the exciton broadening, and μ_T is the reduced trion mass [1]:

$$\frac{1}{\mu_T} = \frac{1}{m_{CB}} + \frac{1}{m_{CB} + m_{VB}} \tag{S3}$$

where m_{CB} and m_{VB} are the effective conduction and valence band masses. The scattering matrices combine as $T = \frac{1}{2}T_s + \frac{3}{2}T_t$, from which we can calculate the self energy Ξ for the case of $E_F < E_b(X^-)$ [1, 2]:

$$\Xi(\hbar\omega, E_F) = \int_0^\infty g_{2D} f_{FD}(E, E_F) T(\hbar\omega + E) \mathrm{d}E \tag{S4}$$

where g_{2D} is the 2D density of states (without spin degeneracy) $m_{CB}/2(\pi\hbar^2)$ and f_{FD} is the Fermi-Dirac distribution:

$$f_{FD}(E, E_F) = \frac{1}{\exp\left(\frac{E-E_F}{k_B T}\right) + 1} \tag{S5}$$

From the self energy we approximate the optical susceptibility [1, 2]:

$$\chi(\hbar\omega, E_F) \approx \frac{-A}{\hbar\omega + i\gamma - E(X^0) - \Xi} \tag{S6}$$

where A is a term accounting for the intervalley optical dipole moment and the exciton wavefunction at $r = 0$, being roughly equivalent to 0.1 in our case [1].

To simulate the absorption of the $MoSe_2$ we plot the imaginary part of the susceptibility in Fig. 1a as a funciton of Fermi level, using $E_b(X^0) = 550$ meV [3], $E_b(X^-) = 25$ meV, $E(X^0) = 1.668$ eV, $\gamma = 3$ meV, $T = 4$ K, $m_{CB} = 0.49$ and $m_{VB} = 0.52$ [4]. It can be seen that as E_F increases, the energy separation between the upper and lower polaron branches increases (Fig. 1b). From the Main Text Fig. 1a, we extract the energy separation at $B = 0$ T between the repulsive and attractive polaron branches as 32.5 meV, and compare this value to Fig. 1b in order to obtain the Fermi level in our $MoSe_2$ monolayer, which we find to be $E_F = (5 \pm 3)$ meV. The large error in E_F arises from the large uncertainty in the trion binding energy in literature, which varies from 21 meV [5] to 30 meV [6]. Here we take an intermediate value $E_b(X^-) = 25$ meV as used by Sidler, *et al.* [7]. Finally, we estimate the free electron density by the 2D density of states with spin degeneracy, $n_e = (m_{CB} m_e E_F)/(\pi\hbar^2)$ and obtain a value $(1.0 \pm 0.6) \times 10^{12}$ cm^{-2}.

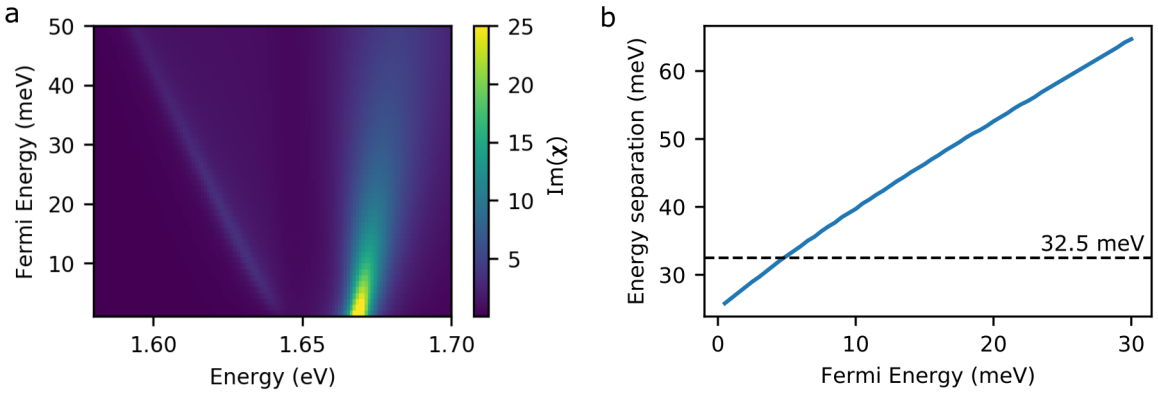

Supplementary Figure 1: (a) Calculated imaginary part of the $MoSe_2$ optical susceptibility at $B = 0$ T as a function of increasing Fermi energy. (b) Energy separation between the exciton and trion (repulsive and attractive polaron branches) as a function of Fermi energy. In our sample the energy separation is 32.5 meV, corresponding to $E_F \sim 5$ meV.

Supplementary Note 2: Theory of the spin dynamics

PHOTOLUMINESCENCE FROM POLARITON MODES

We theoretically describe each circularly polarised trion-polariton mode using a standard two-coupled oscillators model. Since the broadening is significant, we include mode broadening by using an homogenous imaginary part for the bare photon and trion energies [8, 9]. The trion energies are determined by reflection experiments performed on the bare flake. The open cavity mode energy reads as $E_c = \alpha(V + V_0)$ where α the slope of the photonic mode energy versus the applied voltage V controlling the optical cavity length. The upper and lower polariton branch energies read as :

$$E^{\sigma\pm}_{U,LPB} = \frac{1}{2}\,\mathrm{Re}\left(E^{\sigma\pm}_{Ta} + E_c \pm \sqrt{\left(E^{\sigma\pm}_{Ta} - E_c + i\left(\Gamma_{Ta} - \Gamma_c\right)\right)^2 + 4(\Omega^{\sigma\pm})^2}\right) \tag{S7}$$

where $E^{\sigma\pm}_{Ta}$ is the energy of the trion in absorption for a given spin component, $\frac{\Omega^{\sigma\pm}}{2}$ are the Rabi splitting values to be determined, Γ_c=0.6 meV and Γ_{Ta}=6 meV are the measured linewidth of the two modes, which we keep constant.

The trion fractions of the polaritons (square of the Hopfield coefficients) read as:

$$|X^{\sigma\pm}_L|^2 = \frac{4(\Omega^{\sigma\pm})^2}{4\Omega^2 + (E^{\sigma\pm}_{UPB} - E^{\sigma\pm}_{Ta})} \tag{S8}$$

$$|X^{\sigma\pm}_U|^2 = 1 - |X^{\sigma\pm}_L|^2 \tag{S9}$$

These energies are the one which could be measured in a transmission or absorption experiment. As for bare excitons in any media, polaritons demonstrate a finite Stokes shift. In the presence of finite random disorder, the Stokes shift is the difference between the energy of a resonance in absorption which corresponds to the maximum density of states, and in photoluminescence (PL) which corresponds to the lowest energy state of the inhomogeneous distribution of energy resonances. The Stokes shift is quite large in our sample owing to the raised itinerant electron density. Indeed, as the Fermi level increases above the bottom of the conduction band in $MoSe_2$, the Stokes shift will increase as the trion absorption feature blueshifts [7]. As shown in Fig. 1a of the main text, we have performed both reflection and PL measurements on the bare flakes which allows us to precisely determine the bare trion Stokes shift value, which is of the order of 6 meV. It reads

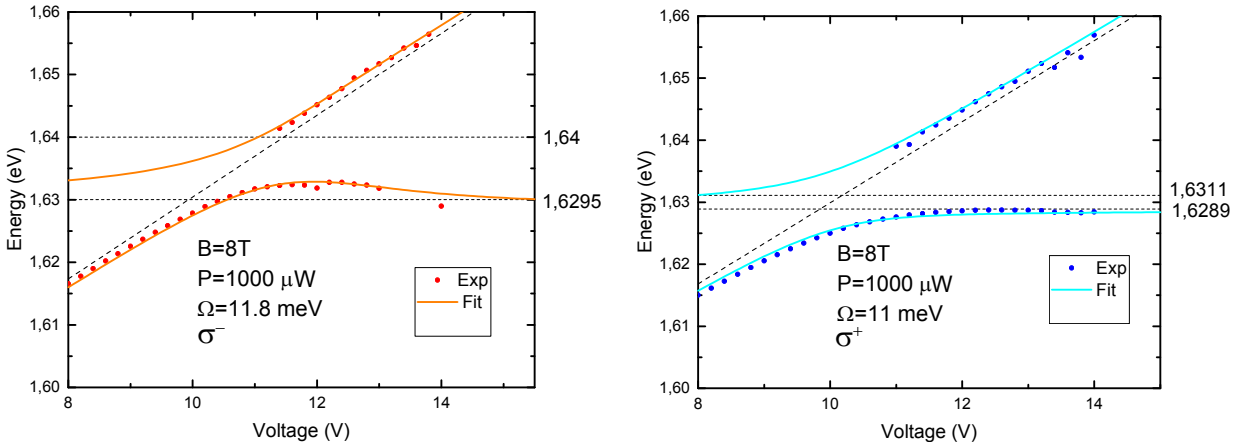

Supplementary Figure 2: Fit of the lower and upper polariton branches in two polarizations: dots – experiment, line – theory.

$$\Delta_S^{\sigma_\pm} = E_{Ta}^{\sigma_\pm} - E_{Te}^{\sigma_\pm} \tag{S10}$$

where $E_{Te}^{\sigma_\pm}$ is the trion energy in PL.

For polaritons, the Stokes shift is reduced with respect the case of the bare trion. The polariton Stokes shift should tend to the trion Stokes shift when the trion fraction of the polariton tends to 1. On the other hand, the Stokes shift should tend to 0 when the polariton becomes strongly photonic. We therefore choose to introduce phenomenologically a polariton Stokes shift value given by:

$$E_{U,L}^{\sigma_\pm} = E_{U,LPB}^{\sigma_\pm} - \Delta_S^{\sigma_\pm} |X_{U,L}^{\sigma_\pm}|^2 \tag{S11}$$

Using the above mentioned formula allows us to fit the voltage-dependence of the trion-polariton PL energies for different pumping powers and magnetic field strengths, with the Rabi splitting in each polarisation being the only fitting parameters. The results are shown in Fig. 1d of the main text and Fig. 2 of the supplementary. The agreement between the experiment and the phenomenological theory which we use is extremely satisfactory. The extracted dependence of the Rabi splitting values versus pumping for both spin components are shown on Fig. 3c of the main text.

MODELLING OF FREE CARRIER DEPOLARISATION

In this section we present the system of rate equations we use in order to compute the free carrier spin polarisation versus pumping power. This model can be used, with different parameters, to describe the relaxation dynamics both in a bare flake and when the flake is embedded in the cavity. In this last case, the computed polarisation degree of carriers (free and those bound to excitons to form trions) allows to directly deduce the dependence of Rabi splitting values versus pumping, and to compare them with the experiment. The scheme of the processes taking place in the system is shown in Suppl. Fig. 3. When pumping starts, the resident carriers are assumed to be all spin-polarized up, because of the applied magnetic field. The pump creates excitons (exciton-polaritons), which bind with the free carriers to form trions (trion-polaritons) with correlated spin. Trions can depolarize a lot faster ($\sim$ ps) than free carriers ($\sim$ ns) because of the L-T spin-orbit coupling (Maialle-Sham mechanism[10, 11]). When these depolarized trions emit light via the exciton recombination and emission of the photon out of the cavity, the remaining free carriers have a reduced polarization. This reduced polarisation depends on the ratio between the trion (trion-polariton) decay time and the trion depolarisation time. The time needed for an electron spin to reorient parallel to the magnetic field is comparable with its depolarisation time ($\sim$ ns). Therefore, even with a small pumping (a few excitons per picosecond), the small number of trions formed by this process can efficiently depolarize a large fraction of free carriers.

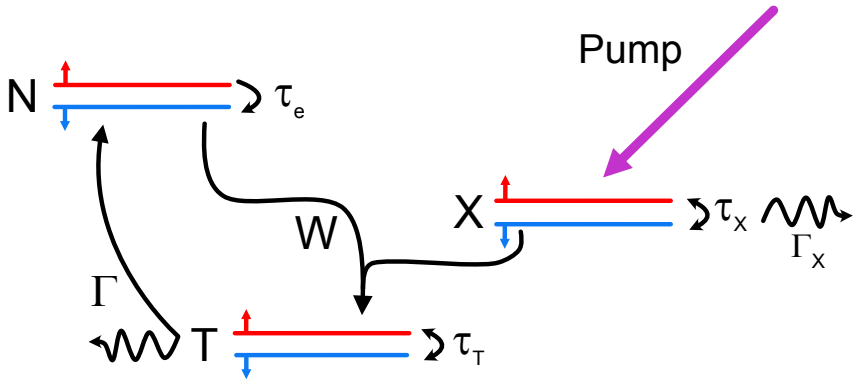

Supplementary Figure 3: Scheme of the population dynamics. Arrows indicate the pumping (violet), scattering and decay rates (black), spin relaxation rates (small black).

The result is that, under optical pumping, we observe strong coupling in a cavity for both polarizations, because there are free carriers of both spins available in the system. The key point is that the effect of the injected exciton density on the Rabi splitting is amplified by the ratio $\tau_e^s/\tau_t^s \sim 10^3$.

Mathematically, the processes described can be modelled by rate equations involving free carriers N, excitons (exciton-polaritons) X, and trions (trion-polaritons) T:

$$\frac{dN_\pm}{dt} = -WN_\pm X_\pm + \Gamma T_\pm \pm \frac{N_-}{\tau_e^s} \mp \frac{N_+}{\tau_e^s} e^{-\frac{\Delta}{k_b T_e}} \tag{S12}$$

$$\frac{dX_\pm}{dt} = -WN_\pm X_\pm + P_\pm - \frac{X_\pm - X_\mp}{\tau_X^s} - \frac{X_\pm}{\tau_X} \tag{S13}$$

$$\frac{dT_\pm}{dt} = WN_\pm X_\pm - \Gamma T_\pm - \frac{T_\pm - T_\mp}{\tau_T^s} \tag{S14}$$

The $\pm$ indices of N, X, and T correspond to the different spins of the free carriers, excitons (exciton-polaritons), and trions (trion-polaritons), respectively.Δ is the electron Zeeman splitting, T_e is the temperature. In all cases, we have considered linearly-polarized pumping: $P_+ = P_-$. The initial number of spin-polarized free carriers is $N_0 = 1000$ (estimated from the density 10^{12} cm^{-2}). The table below gives the parameters we used to describe the bare flake under 0 and 8 T and the cavity system. The trion-polariton decay rate toward a photon and a free electron is $\Gamma = 1/\tau_T$, where τ_T is the trion-polariton's lifetime.

Table of parameters			
Parameter	Bare flake 0T Measured experimentally	Bare flake 8T Fit parameters	Cavity 8T Fit parameters
τ_T		0.2 ps	2 ps
τ_T^s	1 ps	2.7 ps	10 ps
τ_X		0.3 ps	2 ps
τ_X^s	0.2 ps	0.7 ps	5 ps
τ_e^s	3 ns	3 ns	3 ns
Δ	0 meV	3.4 meV	3.4 meV
W		3x10^{-3} ps^{-1}	3x10^{-3} ps^{-1}

The spin lifetimes in the bare flake at 0T have been measured by time resolved spectroscopy, as described in Supplementary Note 4. The parameters used to describe the bare

flake at 8 T have been used to compute the power dependence of the DOCP. The exciton and trion lifetimes correspond to their radiative lifetime, which is proportional to their oscillator strength. This quantity is directly measured from the Rabi splitting value when the flake is embedded in the cavity. Formally, this quantity should depend on the free carrier spin polarisation, but this dependency is neglected. The spin relaxation time of excitons and trions are expected to be longer at 8T than at 0 T, due to the protection offered by the Zeeman splitting. The trion DOCP at low power (around 0.85-0.9) is strongly fixing the ratio between the trion spin lifetime and its radiative lifetime. Suppl. Fig. 4 shows the trion DOCP versus pumping, demonstrating a good agreement between theory and experiment, where increased pumping provokes a depolarisation of the free carrier gas and a decrease of the DOCP. The difference in the trends could be due to the limits of the model, for instance, modelling of the reservoir as a single state.

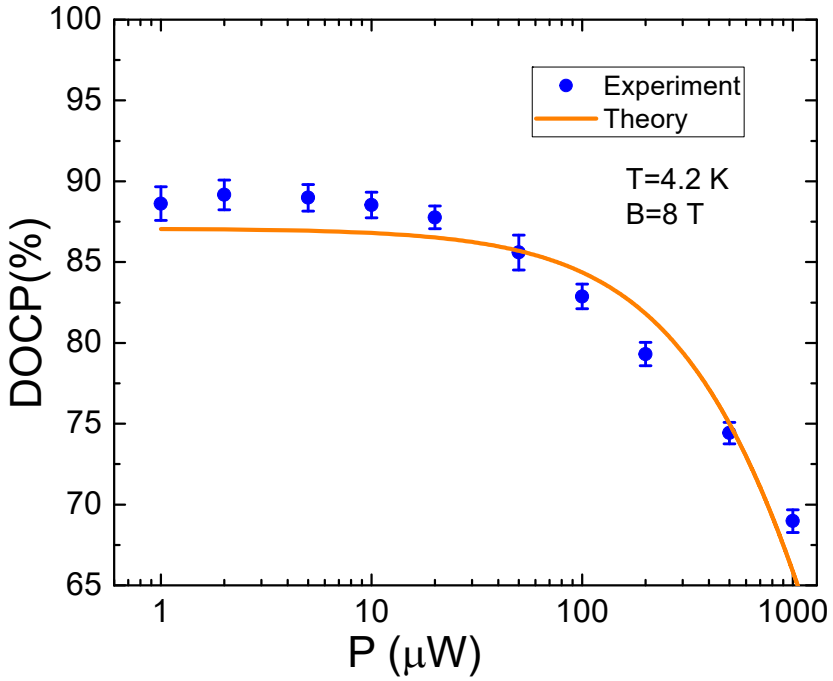

Supplementary Figure 4: Power dependence of the bare flake trion DOCP in photoluminescence at $B = 8$ T. Overlaid is the simulated response. Error bars quantify the uncertainty in peak intensities arising from fitting the trion PL peaks in both polarizations to Lorentzian functions.

In the cavity, the lifetime of the strongly coupled polariton modes is not anymore given by the radiative lifetime of excitons and trions, which now sets the Rabi splitting values.

The trion-polariton and exciton-polariton lifetimes are composed by the decay of the photonic part of the polariton (cavity photon lifetime 1 ps) and the non-radiative decay of excitons/trions. In line with our previous studies [12], we consider a polariton being 50 % photon with a decay rate dominated by the cavity photon lifetime. We also find spin relaxation times substantially larger than in the bare flake. The explanation suggested in [12] is that exciton/trion-polaritons in 0D cavities are constituted by low wavevector excitons with small L-T splitting, which slows down their spin relaxation via to the Maialle-Sham mechanism with respect to a spatially invariant 2D system. In the same way, the elastic disorder scattering is strongly suppressed with respect to the bare trion case, which reduces the disorder contribution to the decay and makes the polariton decay rate dominated by the photonic part of the polariton.

With all the parameters describing the cavity (different from those of the bare flake), we compute the steady state populations of all species versus pumping power. This allows to determine the oscillator strength of the bare trion resonance for each spin, which is proportional to the density of carriers with the same spin [13]. The Rabi splitting is proportional to the square root of the oscillator strength [9]. For a given polarisation, it is therefore proportional to the square root of the number of carriers of the corresponding spin (both free and bound in trions). Fig. 3c of the main text shows the change of the Rabi splitting of each polarisation versus pumping computed with the above mentioned model compared with the experimentally extracted data. The agreement is very satisfactory. Finally, we compute the effective trion-polariton interaction strength. By definition, the interaction constant is given by $\alpha = \partial E^{+}_{LPB}/\partial n^{+}$, where E^{+}_{LPB} is the lower polariton branch energy for the σ^{+} polarization calculated with equation (S7) and n^{+} is the particle density corresponding to the pumping value P. This correspondence is determined by the free electron density, discussed in the Supplementary Note 1, and by the fitting parameters, summarized in the Table above. Fig. 3c (middle panel) of the main text shows the evolution of the effective interaction α versus the pumping power for a given magnetic field $B = +8T$. The high value of the interaction constant is qualitatively explained by the high ratio of the spin relaxation times, allowing a small density of excitons to depolarize the free electrons thus strongly affecting the polariton energy via the Rabi splitting. The procedure for the calculation of the uncertainty of the effective interaction is as follows. The rate equation model allows one to get the Rabi and the effective interaction for a set of parameters, whose values are given

in the data table. We then change systematically all parameters, keeping the Rabi value within the experimental error bars. We find that α is mostly sensitive to the trion lifetime and that it does not vary by more than 25% of its nominal value, which we define as the uncertainty for the effective interaction indicated in the main text.

Supplementary Note 3: Enhanced valley splitting of $MoSe_2$ on EuS substrates

The sample used in this work consists of a $MoSe_2$ monolayer in direct contact with a 10 nm thick europium sulfide (EuS) thin film. We confirm the ferromagnetism of this film by vibrating-sample magnetometry with an in-plane B-field, where clear magnetization saturation and hysteresis is seen (Fig. 5a). In recent years, monolayer TMDs on EuS substrates have been shown to exhibit an enhanced valley Zeeman splitting in the fundamental exciton absorption peak, attributed to the interfacial magnetic exchange field [14–16]. In our sample, an enhanced and nonlinear valley splitting of the neutral exciton X_{RC} (repulsive polaron) is also observed, however, the enhancement is not seen in the valley splitting of the trion PL peak T_{PL}, which shifts with applied field at a rate of 0.23 meV / T, consistent with the conventional valley Zeeman effect in $MoSe_2$ (Fig. 5b) [17]. As the PL valley splitting is a better reflection of the energy shifts of the band edges under a B-field than the RC valley splitting, we rule out an interfacial exchange field induced valley splitting of $+K$ and $-K$ band edges. Instead, we interpret the enhanced valley splitting seen in X_{RC} as being due to state filling as the raised free carrier population in the flake redistributes between conduction band valleys, thereby enlarging the photon absorption energy. This is additionally supported when we consider the enhancement to the valley splitting of X_{RC}, by subtracting a linear shift of 0.23 meV / T from the measured splitting. This is plotted in Fig. 5d overlaid with the DOCP of T_{RC}, where it can be seen that both curves follow exactly the same response to the applied external B-field. This strongly suggests that the enhancement to the valley splitting of X_{RC} and the DOCP of T_{RC} both arise from the redistribution of free electrons between the conduction band valleys as the valley degeneracy is lifted by the applied B-field.

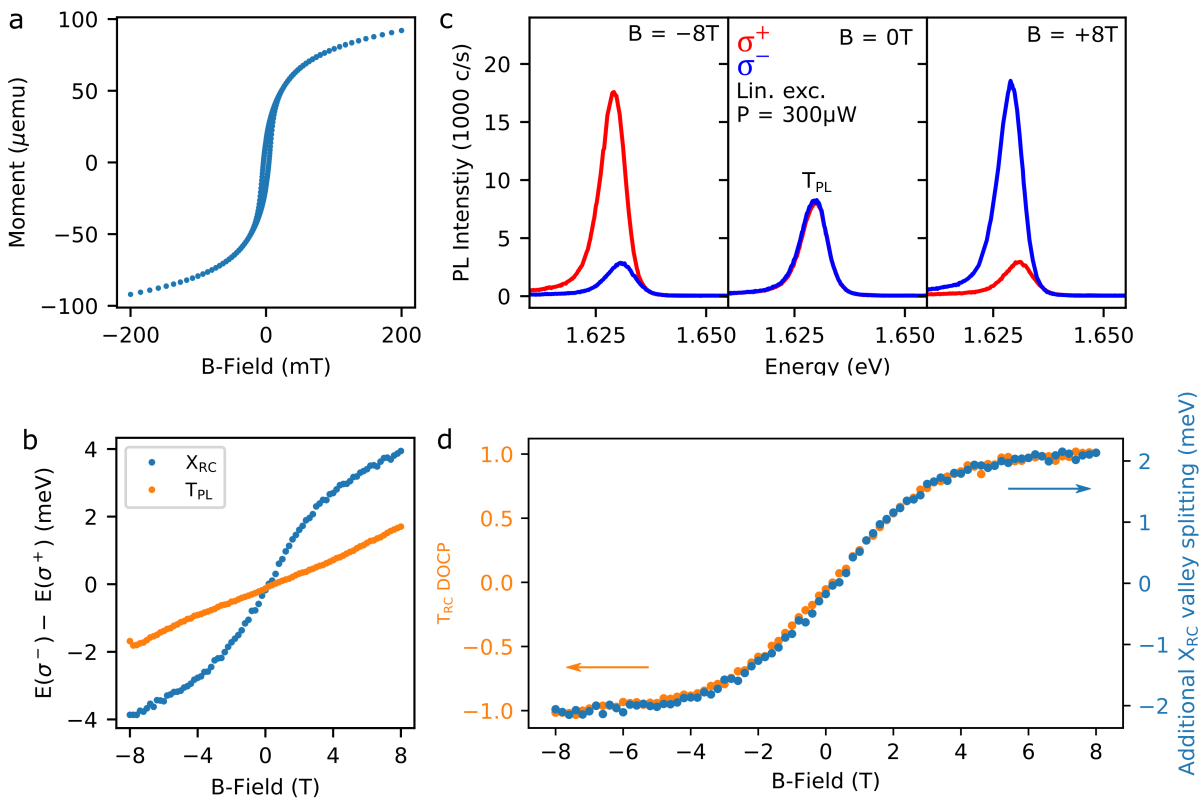

Supplementary Figure 5: (a) Vibrating-sample magnetometer (VSM) data from the EuS film used in this work, showing clear signatures of ferromagnetism. The B-field is applied in the sample plane and the sample temperature is 4 K. (b) The valley splitting (here defined as $E(\sigma^-) - E(\sigma^+)$) of X_{RC} and T_{PL}, showing that while X_{RC} displays an enhanced and non-linear valley splitting, T_{PL} does not. (c) Trion PL spectra from the bare flake at B= $-8, 0, +8$ T, under non-resonant laser excitation. (d) Comparison between the enhancement to the X_{RC} valley splitting (calculated as the measured X_{RC} valley splitting minus a linear shift of 0.23 meV / T arising from the valley Zeeman effect caused by the externally applied B-field) and the DOCP of T_{RC}. The exact match between the two B-field responses supports the conclusion that both effects arise from the same origin, that of 2DEG redistribution between valley states.

Supplementary Note 4: Time resolved spectroscopy of monolayer $MoSe_2$ on EuS substrates

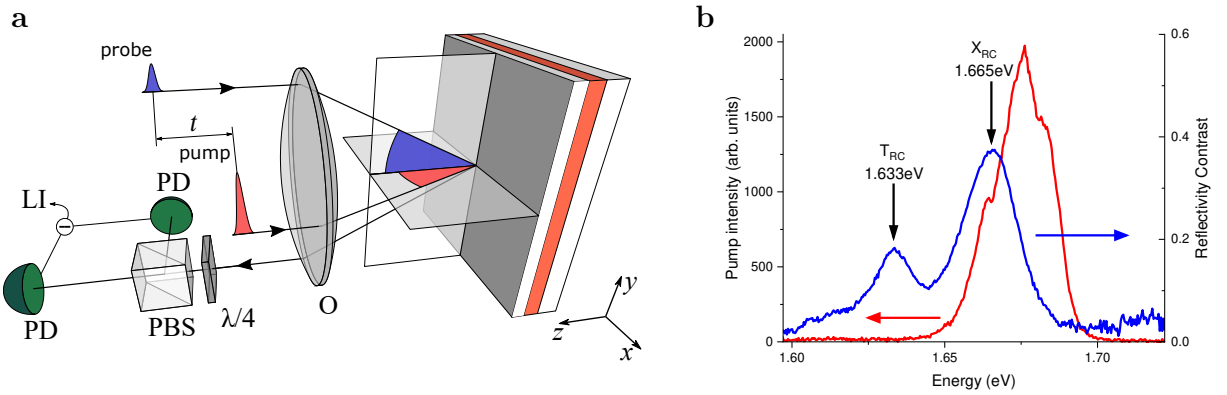

Supplementary Figure 6: (a) Illustration of the pump-probe system used for these measurements. O is the microscope objective, $\lambda/4$ the quarter-wave plate, PBS the polarizing beam splitter, PD are the balanced photodetectors and LI is the lock-in amplifier. (b) Comparison of the reflectance contrast ($\Delta R/R$) spectrum from Sample 2 with the pump spectrum, quasi-resonant with the neutral exciton transition.

We have studied spin dynamics using the time resolved pump-probe ellipticity technique on a second $MoSe_2$ / EuS sample, which we call Sample 2. Reflectance contrast measurement of the monolayer reveals a spectrum similar to sample 1 presented in the main text, with two strong absorption features corresponding to the neutral exciton X_{RC} (repulsive polaron) at higher energy and trion T_{RC} (attractive polaron) at lower energy.

For the time resolved pump-probe measurements (setup shown schematically in Fig. 6a), we use laser pulses which are generated by a Ti:sapphire oscillator with a central wavelength of 790 nm, a spectral width of about 100 nm, and a repetition rate of 80 MHz. The laser beam travels through a pulse shaper and a compressor, which are used to compensate the pulse chirp acquired during propagation through the optical elements before reaching the sample. The resulting spectrum is centered around 765 nm (1.62 eV) with a full-width at half maximum (FWHM) of about 45 nm (100 meV). After that the laser beam is divided by a silica beam splitter into the pump and probe beams. The temporal delay t between the pump and probe pulses is adjusted by a motorized mechanical delay line mounted in

the pump beam path. The intensity of the pump beam is modulated using a mechanical chopper at the frequency of 2.1 kHz.

In order to perform two-color pump-probe experiments each of the two beams is spectrally narrowed before focusing at the sample using interference bandpass filters. For pump pulses the center wavelength is set fixed at 740 nm (1.675 eV) with 10 nm bandwidth, leading to the photoexcitation of excitons in the K valley of $MoSe_2$. The probe beam has wavelength selectivity provided by a tunable bandpass filter with FWHM of 7 nm in the excitation path, allowing a combination of time and spectrally resolved measurements. A comparison of the pump spectrum with the sample reflectance contrast spectrum (acquired with spectrally broad probe beam only, i.e. without using the tunable filter in the excitation path) is shown in Fig. 6b. The duration of the pump and probe pulses are about 80 and 120 fs providing the overall time-resolution of about 150 fs.

The laser beams are focused at the sample surface into spots with diameters of about 20 μm using a single microscope objective (10$\times$ magnification with numerical aperture of 0.26). The pump power is set to 100 μW while the probe power varies from 1 to 10 μW depending on the central wavelength, i.e. the probe intensity is at least $\sim 10\times$ weaker than the pump. The incidence angles for the pump and probe are 10° and 7° in the horizontal (zx) and vertical (zy) planes, respectively, as shown in Fig. 6(a). The reflected beams are collected by the same objective. Then the probe beam is guided into the polarization bridge setup equipped with a polarizing beam splitter (PBS) and balanced photodetectors (PDs) [see Fig. 6(a)]. The pump beam is circularly polarized, while the probe is linearly polarized. An additional quarter-wave plate is used before the PBS in order to measure the ellipticity signal, i.e. the difference between σ^+ and $\sigma-$ polarized components of the reflected probe beam. The PD signal is detected using a lock-in amplifier synchronized at the pump modulation frequency. The resulting ellipticity signal reveals the time decay of the difference in σ^+ and σ^- circularly polarized absorption from the sample, which is proportional to the pump induced spin polarization of photoexcited and resident carriers.

Fig. 7 shows the results of the time resolved pump-probe spectroscopy. Each transient is normalized by the intensity of the probe beam for each particular probe photon energy $\hbar\omega_{\mathrm{probe}}$. Figure 7a shows the transient ellipticity on long (100s ps) timescales, in which a clear offset from zero can be seen when the probe is close to resonance with the trion state at 1.636 eV. This implies a long spin relaxation component, which we fit to be ~ 3 ns, and at-

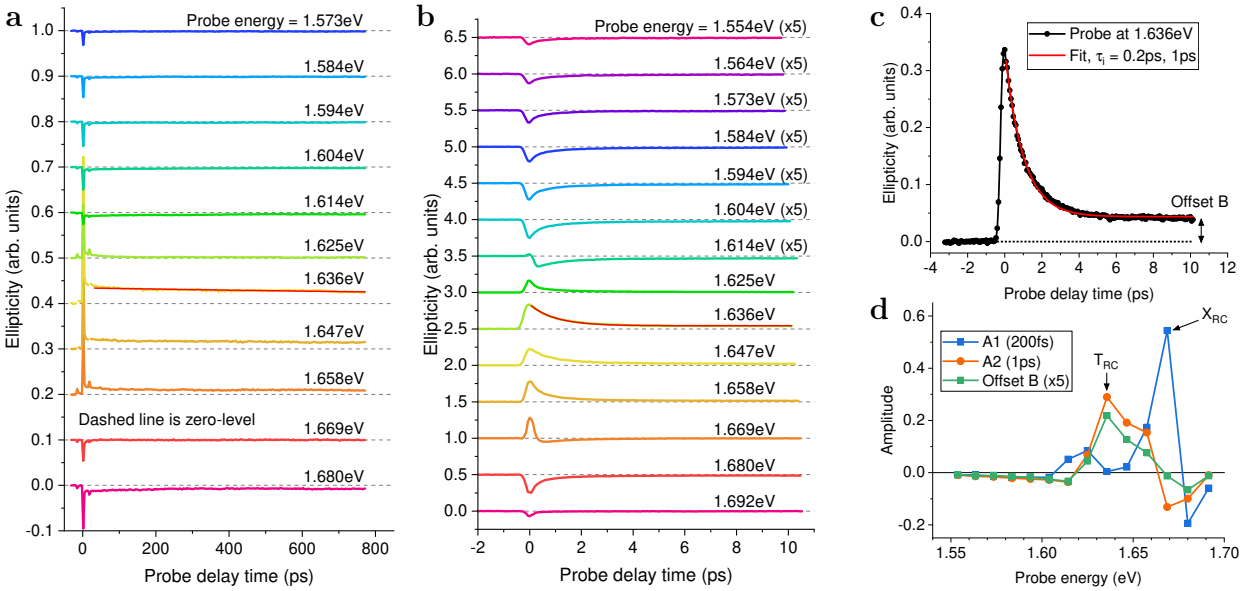

Supplementary Figure 7: (a,b) Transient ellipticity (quantifiying the difference between σ^+ and σ^- reflectivity) over long (a) and short (b) timescales, for various probe energies. A very long decay component, fitted to $\sim$ 3 ns, can be seen in (a) when the probe is resonant with the trion state (1.636 eV), while on shorter timescales, the trion shows a biexponential decay (b). (c) Example of biexponential fitting to the transient ellipticity with the probe at 1.636 eV. The two timescales are 200 fs and 1 ps. The long ($\sim$ 3 ns) decay component can be seen as a clear offset from zero. (d) Amplitudes of the two components of the biexponential decay, and the offset / long decay versus probe energy. The 200 fs decay is strongest at the neutral exciton energy (1.665 eV) while the 1 ps and 3 ns decays are strongest at the trion energy.

tribute to the spin relaxation of the free electrons constituting the 2DEG [18]. Fig. 7b shows the measurement on a much shorter timescale (few ps), in which we observe a biexponential decay of the ellipticity. We fit these data with a biexponential curve superimposed on a constant offset B from zero (see Fig. 7c) $A_1 \exp\left(-\frac{t}{\tau_{s1}}\right) + A_2 \exp\left(-\frac{t}{\tau_{s2}}\right) + B$, which accounts for the long-lived spin relaxation component seen in Fig. 7a. This assumption is valid on the timescales considered here. From data fits at different energies $\hbar\omega_{\text{probe}}$ it follows that there are two characteristic timescales with spin relaxation times $\tau_{s1} = 200$ fs and $\tau_{s2} = 1$ ps. The spectral dependence of A_1 and A_2 associated with the biexponential decay is extracted as a function of $\hbar\omega_{\text{probe}}$ and plotted alongside the long-lived decay B in Fig. 7d. Here it can be seen that the maximum amplitude of $A_1(\hbar\omega_{\text{probe}})$ occurs when the probe is resonant

with the neutral exciton (1.665 eV), while $A_2(\hbar\omega_{\text{probe}})$ and the offset $B(\hbar\omega_{\text{probe}})$ both reach maximum values when the probe is resonant with the trion state (1.635 eV). This allows us to assign three contributions in the following way: A_1 with $\tau_{s1} = 200$ fs to neutral exciton spin relaxation, A_2 with $\tau_{s2} = 1$ ps to trion spin relaxation, and the offset value B with decay constant of ~ 3 ns to the 2DEG spin relaxation [18]. This result corroborates our theoretical model presented in Supplementary Note 2 to explain the spin dynamics of the $MoSe_2$ microcavity system.

Supplementary Note 5: Low temperature magneto-optical spectroscopy in a tunable micro-cavity

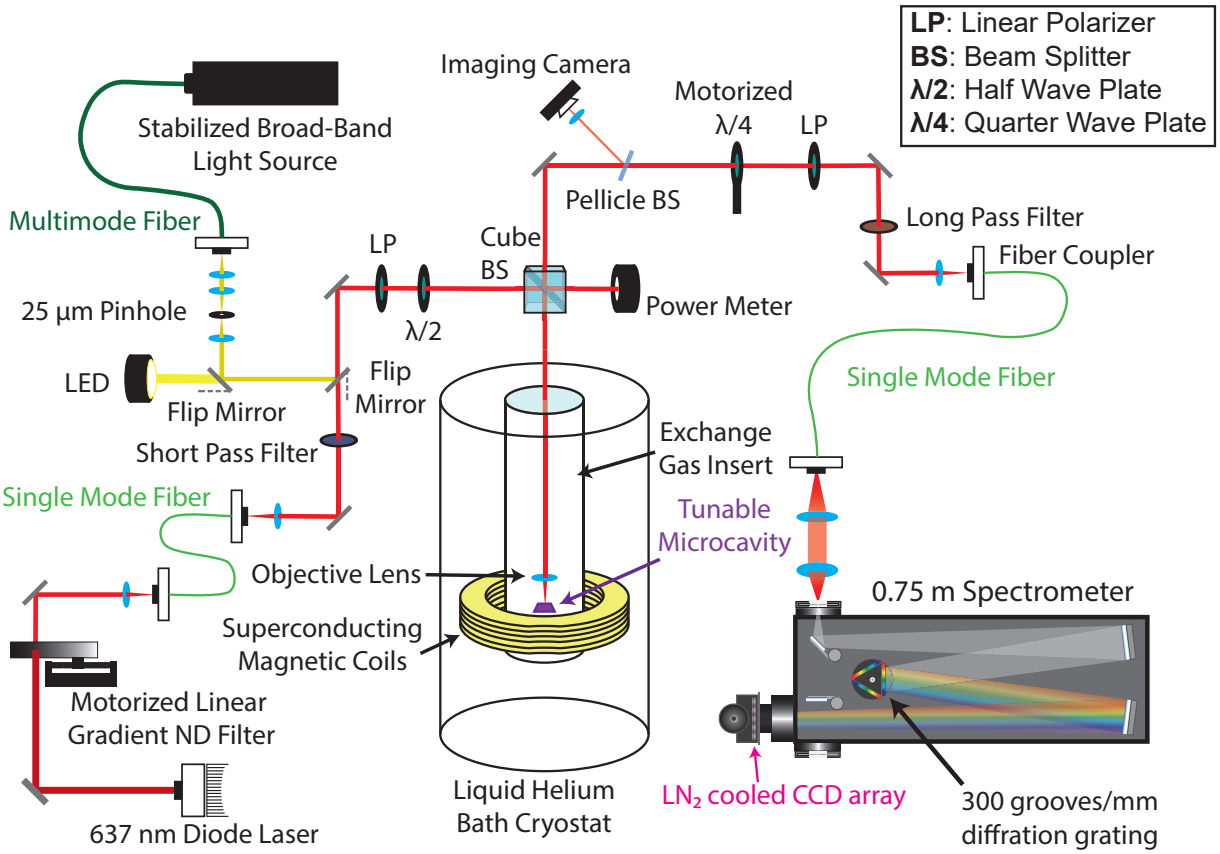

Supplementary Figure 8: Schematic of the experimental setup used for low temperature polarisation resolved spectroscopy, including beam paths for the photoluminescence, reflectivity, and live imaging along with the required polarisation optics. Abbreviations are detailed in the legend.

[1] Roch, J. G. *et al.* Spin-polarized electrons in monolayer MoS_2. *Nature Nanotechnology* **14**, 432–436 (2019).

[2] Suris, R. A. *et al.* Excitons and Trions Modified by Interaction with a Two-Dimensional Electron Gas. *Physica Status Solidi (B)* **227**, 343–352 (2001).

[3] Ugeda, M. M. *et al.* Giant bandgap renormalization and excitonic effects in a monolayer transition metal dichalcogenide semiconductor. *Nature Materials* **13**, 1091–1095 (2014).

[4] Wang, G. *et al.* Magneto-optics in transition metal diselenide monolayers. *2D Materials* **2**, 034002 (2015).

[5] Berkelbach, T. C., Hybertsen, M. S. Reichman, D. R. Theory of neutral and charged excitons in monolayer transition metal dichalcogenides. *Physical Review B* **88**, 045318 (2013).

[6] Ross, J. S. *et al.* Electrical control of neutral and charged excitons in a monolayer semiconductor. *Nature Communications* **4**, 1474 (2013).

[7] Sidler, M. *et al.* Fermi polaron-polaritons in charge-tunable atomically thin semiconductors. *Nature Physics* **13**, 255–261 (2017).

[8] Savona, V., Andreani, L. C., Schwendimann, P. Quattropani, A. Quantum well excitons in semiconductor microcavities: Unified treatment of weak and strong coupling regimes. *Solid State Communications* **93**, 733–739 (1995).

[9] Kavokin, A. Malpuech, G. *Cavity polaritons.* (Elsevier, 2003).

[10] Maialle, M. Z., de Andrada e Silva, E. A. Sham, L. J. Exciton spin dynamics in quantum wells. *Physical Review B* **47**, 15776-15788 (1993).

[11] Glazov, M. M. *et al.* Exciton fine structure and spin decoherence in monolayers of transition metal dichalcogenides. *Physical Review B* **89**, 201302 (2014).

[12] Dufferwiel, S. *et al.* Valley-addressable polaritons in atomically thin semiconductors. *Nature Photonics* **11**, 497–501 (2017).

[13] Emmanuele, R. P. A. *et al.* Highly nonlinear trion-polaritons in a monolayer semiconductor. *Nature Communications* **11**, 3589 (2020).

[14] Norden, T. *et al.* Giant valley splitting in monolayer WS_2 by magnetic proximity effect. *Nature Communications* **10**, 4163 (2019).

[15] Zhao, C. *et al.* Enhanced valley splitting in monolayer WSe_2 due to magnetic exchange field.

Nature Nanotechnology **12**, 757–762 (2017).

[16] Scharf, B., Xu, G., Matos-Abiague, A. Žutić, I. Magnetic Proximity Effects in Transition-Metal Dichalcogenides: Converting Excitons. *Physical Review Letters* **119**, 127403 (2017).

[17] MacNeill, D. *et al.* Breaking of Valley Degeneracy by Magnetic Field in Monolayer $MoSe_2$. *Physical Review Letters* **114**, 037401 (2015).

[18] Schwemmer, M., Nagler, P., Hanninger, A., Schüller, C. Korn, T. Long-lived spin polarization in n-doped $MoSe_2$ monolayers. *Applied Physics Letters* **111**, 082404 (2017).